The Astrophysical Journal, 731:89 (11pp), 2011 April 20 doi:10.1088/0004-637X/731/2/89

THE FAINT STELLAR HALOS OF MASSIVE RED GALAXIES FROM STACKS OF MORE THAN 42,000 SDSS LRG IMAGES

Tomer Tal and Pieter G. van Dokkum
Astronomy Department, Yale University, P.O. Box 208101, New Haven, CT 06520-8101, USA
Received 2010 September 7; accepted 2011 February 19; published 2011 March 28

ABSTRACT

We study the properties of massive galaxies at an average redshift of $z \sim 0.34$ through stacking more than 42,000 images of luminous red galaxies (LRGs) from the Sloan Digital Sky Survey (SDSS). This is the largest data set ever used for such an analysis and it allows us to explore the outskirts of massive red galaxies at unprecedented physical scales. Our image stacks extend farther than 400 kpc, where the r-band profile surface brightness reaches 30 mag arcsec^{-2}. This analysis confirms that the stellar bodies of LRGs follow a simple Sérsic profile out to 100 kpc. At larger radii, the profiles deviate from the best-fit Sérsic models and exhibit extra light in the r-, i-, and z-band stacks. This excess light can probably be attributed to unresolved intragroup or intracluster light or a change in the light profile itself. We further show that standard analyses of SDSS-depth images typically miss 20% of the total stellar light and underestimate the size of LRGs by 10% compared to our best-fit r-band Sérsic model of $n = 5.5$ and $r_e = 13.1$ kpc. If the excess light at $r > 100$ kpc is considered to be part of the galaxy, the best-fit r-band Sérsic parameters are $n = 5.8$ and $r_e = 13.6$ kpc. In addition, we study the radially dependent stack ellipticity and find an increase with radius from $\epsilon = 0.25$ at $r = 10$ kpc to $\epsilon = 0.3$ at $r = 100$ kpc. This provides support that the stellar light that we trace out to at least 100 kpc is physically associated with the galaxies themselves and may confirm that the halos of individual LRGs have higher ellipticities than their central parts. Lastly, we show that the broadband color gradients of the stacked images are flat beyond roughly 40 kpc, suggesting that the stellar populations do not vary significantly with radius in the outer parts of massive ellipticals.

Key words: galaxies: elliptical and lenticular, cD – galaxies: evolution – galaxies: interactions – galaxies: structure

Online-only material: color figures

1. INTRODUCTION

Elliptical galaxies dominate the galaxy mass function for $M_\star \geqslant 10^{11} M_\odot$ and are the brightest extended objects in the nearby universe. Extensive effort has been made to study nearby ellipticals, relying on observations of their morphology, kinematics, and stellar populations (e.g., Faber & Jackson 1976; Illingworth 1977; Boroson et al. 1983; Dressler et al. 1987; Kormendy & Djorgovski 1989; Peletier 1989; Worthey et al. 1992). Most studies have focused on the bright centers of these galaxies, out to 1–2 effective radii, as detection of their faint outskirts has posed a challenge both observationally and analytically. Nevertheless, there exists great interest in correctly analyzing the full physical extent of massive red galaxies, particularly as they may build up inside-out through mergers (Loeb & Peebles 2003; Naab et al. 2007; Bezanson et al. 2009). An accurate measurement of the light profile shape of low-redshift galaxies is crucial for the interpretation of high-redshift galaxy observations.

Direct observations of the outskirts of individual massive galaxies are hard to perform given the extremely faint surface brightness level that is reached at large radii. The observed light in such data is highly influenced by nearby objects, flat-fielding errors, and the wings of the point-spread function (PSF; e.g., Caon et al. 1990; Mihos et al. 2005; de Jong 2008; Tal et al. 2009; van Dokkum et al. 2009). A recent study by Kormendy et al. (2009) utilized a compilation of data from several sources including observations of 28 Virgo ellipticals. The authors detected light outside of five effective radii in only two galaxies, M87 and M49, which are the most luminous Virgo galaxies. There have also been many studies of extended light distributions in massive clusters, and in those environments the light at large distances from the central galaxy is usually attributed to an intracluster stellar population distinct from the central galaxy (intracluster light, or ICL). The ICL has been successfully traced to distances of >500 kpc in several studies (e.g., Gonzalez et al. 2000; Krick & Bernstein 2007; Mihos et al. 2005).

As an alternative to deep observations, stacking a large number of images of similar galaxies could greatly improve the reached overall depth at the cost of losing system specific information. This technique has been used by several authors in studies of both spiral and elliptical galaxies (e.g., Zibetti et al. 2004; van Dokkum et al. 2010). Zibetti et al. (2005, hereafter Z05) stacked 683 images of clusters in the Sloan Digital Sky Survey (SDSS) and reported that the ICL accounts for 10% of the total light in galaxy clusters.

In this study, we stack an unprecedentedly large sample of luminous red galaxy (LRG) images, in a similar way as Z05, to explore the faint outskirts of massive red galaxies. LRGs are thought to be mostly group centrals that live in lower mass halos than the objects studied in Z05. By stacking the LRG data, we hope to shed new light on the properties of these objects at very large radii and to better constrain the size and total luminosity of elliptical galaxies at $z \sim 0.34$.

2. LRG IMAGE STACKING

2.1. Sample Selection

We selected galaxy images for this study from SDSS (Abazajian et al. 2009) including all objects classified as LRGs that have a spectroscopic redshift measurement. LRGs are intrinsically red and luminous objects that were identified as such from their central surface brightness and location on a rotated color–color diagram (for full details see Eisenstein et al. 2001). This selection is aimed at finding the most luminous red galaxies in the nearby universe ($L \geqslant 3L^\star$) out to a redshift of $z = 0.5$.

Being some of the most massive galaxies in SDSS, LRGs occupy the high end of the stellar mass spectrum between $10^{11}\ M_{\odot}$ and a few times $10^{12}\ M_{\odot}$. Roughly 90% of all LRGs are central halo galaxies and they mainly reside in groups with a typical halo mass of a few times $10^{13}\ M_{\odot}$ (Wake et al. 2008; Zheng et al. 2009; Reid & Spergel 2009).

The seventh data release of SDSS (DR7) includes 188,366 spectroscopic LRGs over a wide range of redshifts and apparent magnitudes. The redshift distribution has two main populations peaking at $z \sim 0.05$ and $z \sim 0.34$. The lower redshift LRG candidates are predominantly a contamination sub-sample of fainter, lower mass red galaxies. In order to assure that our sample is indeed composed of high mass LRGs, we selected objects with a narrow distribution of redshifts around the high-z peak. This selection also ensures that galaxies in this distance and brightness ranges do not suffer from significant size and mass evolution within the sample.

The main sample used in this study comprises 55,650 galaxies in a redshift range $0.28 \leqslant z \leqslant 0.40$ with a mean redshift $< z > = 0.34$, resulting in an apparent r-magnitude range of 18.5 ± 0.4 (Figure 1). In fact, 99% of the sample falls within the flux limit of cut I, as defined by Eisenstein et al. (2001), making it approximately volume limited. From this master list, we excluded 12,750 galaxies (23%) where more than 75% of the central $5'' \times 5''$ had to be masked out due to close proximity to another object (masking details in Section 2.2). In addition, we excluded 293 (<1%) of the LRGs because of varying sky levels in the frame caused by close proximity to a bright star in or just outside of the field. Finally, we excluded 28 (<0.1%) images of galaxies with apparent r-magnitude outside of the selected range (details in Section 2.3). The final sample consists of 42,579 galaxies.

2.2. Preparing the Images for Stacking

We acquired imaging data for the fields containing the selected galaxies from the SDSS archive in all five bands: u, g, r, i, and z, corresponding to central wavelengths of 355.1 nm, 468.6 nm, 616.5 nm, 748.1 nm, and 893.1 nm, respectively. For each selected object, we cut out a square region of roughly $200'' \times 200''$ (950 kpc at $z = 0.34$), centered on the galaxy, from the five *ugriz* field images. We then shifted the resulting thumbnails using cubic convolution interpolation to center the main galaxy on the central pixel. Parts of the resulting thumbnails which extended beyond the SDSS stripe edge where given zero weight in the stacked images.

In order to detect and mask out any foreground and background objects, we created a masking template by combining the thumbnails of three of the optical bands (r, i, and z). This increased the signal-to-noise ratio (S/N) of the template by a factor of roughly $\sqrt{3}$ compared to the individual frames, thus enabling us to unveil more sources in the field. We then ran SExtractor (Bertin & Arnouts 1996) on the combined image and detected all the objects in the frame. We set the detection threshold to a value of 1.4 times the standard deviation above the background rms level and used AUTO photometry to extract Kron radii for the detected objects. Finally, we constructed elliptical object masks by growing the semimajor and semiminor axes as determined by SExtractor by a factor of 2.5. We found the optimal values for both the detection threshold and the mask growth factor from trial and error and verified that no additional unmasked objects remained in a visual inspection of the images (Figure 2). The resulting masks cover on average 18% of the total area of each thumbnail. We note that galaxies below the detection threshold of SDSS are not excluded by our procedure. We return to this in Section 2.4.

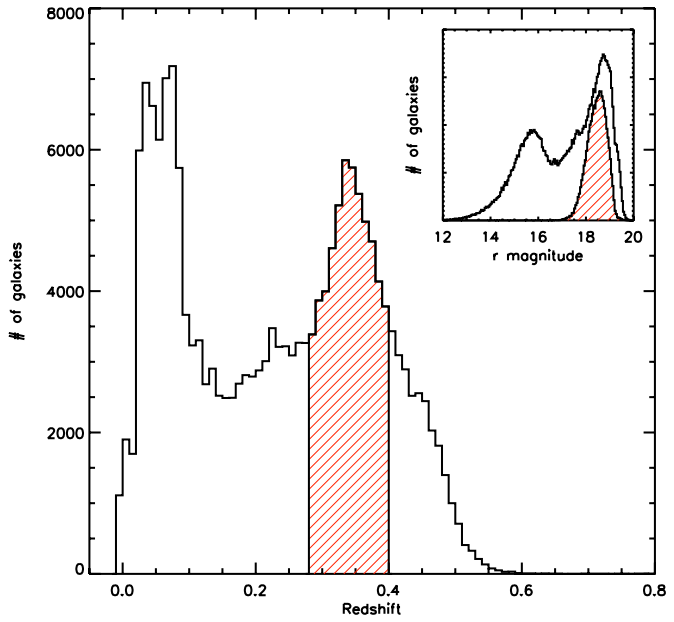

Figure 1. Redshift distribution of the entire LRG candidate sample (black contour) overlaid with the cuts applied in this study (red area). The mean value of the selected sample is $z \sim 0.34$. The resultant r-magnitude distribution is also shown, along with the overall LRG r-magnitude distribution, in the top-right corner.

(A color version of this figure is available in the online journal.)

2.3. Magnitude-bin Stacks

After creating object masks using the combined $g + r + i$ images, we continued on to preparing the individual band images for stacking. We did so by applying the master mask to the images in each of the bands and carefully subtracting both the soft bias, as introduced by the SDSS pipeline, and the remaining sky from the images. We determined the background sky level by temporarily masking out the central galaxy and fitting a Gauss curve to the pixel distribution of each masked thumbnail, assuming that the residual sky pixel values are distributed like Poisson noise. This resulted in a set of five thumbnails per field with the central LRG being the only light source in each sky-subtracted frame. We compared the background level values we found to those obtained from the image headers, where those were available, and found excellent agreement.

One of the challenging aspects of stacking images with any range of object brightnesses lies in the normalization of individual frames in respect to one another. To minimize normalization errors and optimize the S/N, we did not normalize each individual image but rather divided the sample into 13 bins based on the apparent magnitude of the galaxies as determined by the SDSS pipeline. By doing so we ensured that the galaxies in each bin are "pre-normalized." The bins span a brightness range of 17–19.6 r-magnitudes at intervals of 0.2 mag, corresponding to a flux difference of up to only 20% within any given bin. These magnitude cuts were chosen such that only bins that had at least 100 galaxies in them will be processed. We note that we did not rescale the images to a common physical scale prior to stacking them. The ±10% variation in physical scale over the redshift range of the sample is likely small compared to the variation in effective radii between the individual galaxies.

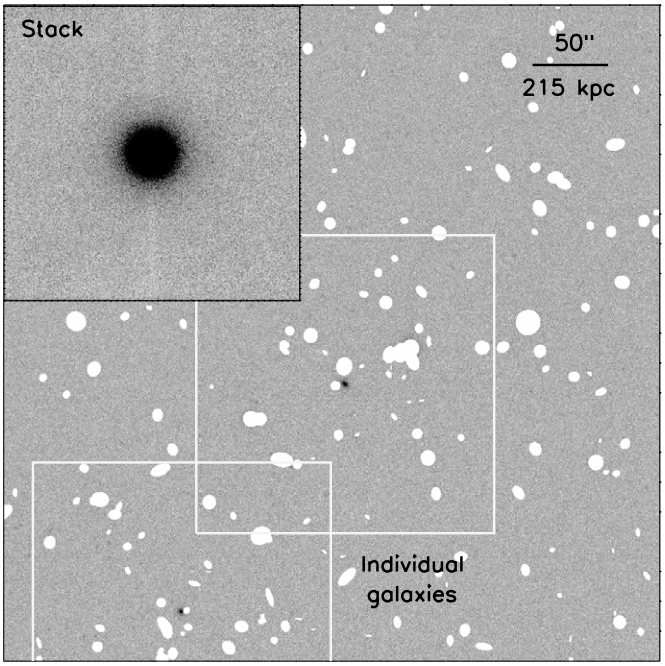

Figure 2. Image preparation for stacking: thumbnails of size $200'' \times 200''$ pixels were cut around each LRG while all other objects in the field were masked out. The stack in the top-left corner was made using more than 42,550 LRG images and can be traced to a radius greater than 100 kpc.

In addition to stacking masked, LRG centered images within each magnitude bin we summed up their corresponding object masks to serve as weight maps for the stacks. We then divided the summed images in each of the five bands by their respective weight mask, thus creating an averaged exposure-corrected stack. Since no normalization was required for images within the same magnitude bin, the noise characteristics were essentially improved by the square root of the number of images in that bin.

2.4. Random Stacks

Correct sky subtraction is crucial for properly analyzing the faint outskirts of the galaxy stacks. However, since the residual "sky" is actually composed of at least three different light sources, the background subtraction performed in Section 2.3 has little physical meaning. These light sources include "real" sky background, light from undetected, and therefore unmasked, galaxies and—most importantly—light from the faint outer halo of the central LRG. In order to obtain a meaningful background measurement, we stacked thumbnails at random locations within fields from the stacking list, using the same number of frames as are in the galaxy stacks and the exact same sky level values as determined for individual fields in the previous step. For each of the optical bands, we created 100 random stacks in every magnitude bin to achieve a statistically meaningful distribution of the noise characteristics. We then averaged the random stacks and subtracted the resulting image from each of the magnitude-bin stacks. The background in the LRG stack is now defined as all emission in the vicinity of the LRG in excess of that of a random, nearby position.

2.5. Final Steps

As a last step prior to averaging the magnitude-bin stacks, we normalized them with respect to each other using the mean apparent magnitude of their input images. We then summed the normalized stacks, weighting them by their relative total number of stacked frames. Finally, for the purpose of absolute photometry calibration, we matched the final stack to the average apparent magnitude of the $18.0 \leqslant m_r < 18.2$ bin, resulting in five photometrically calibrated stacks in the u, g, r, i, and z bands. We note that this method of normalizing magnitude-binned stacks is significantly less sensitive to photometry errors than normalizing individual images.

3. STACK ANALYSIS

Each of the 42,579 frames that went into making the final stack was obtained with 53.9 s of exposure time. The final stacks, then, have an effective depth that corresponds to an exposure time of roughly 2.3 Ms, equivalent to 40 hr on a 10 m class telescope. Obviously, such deep images of individual objects would be completely dominated by light from neighboring objects, flat-field errors, and scattered light by the PSF. Stacking a large number of images may currently be the best method for studying the faint outskirts of galaxies.

3.1. PSF Stacks

When analyzing any deep data set, one must be aware of the effects of light scatter due to the PSF in the images. Since the dynamic range in the data is large, the faint outskirts of the stack can in fact be dominated by scattered light from the bright galactic center. In order to determine the effects of the PSF on the galaxy stacks and to properly remove them, we stacked synthesized PSF images created using Robert Lupton's Read Atlas Images code.[1] The PSF images were produced at the same CCD positions as the stacked LRG images for each of the observed bands. However, the synthetic PSFs only extend as far as $\sim 12''$ (58 kpc) in radius and do not reach the full extent of the LRG stacks, where PSF "contamination" may still be important (see, for example, de Jong 2008; Bergvall et al. 2010). We therefore stacked all the bright star images from SDSS in the r-magnitude range $8.0 < m_r < 8.2$ in each of the five optical bands. The resulting stacks are saturated inside of roughly $5''$, where they are unusable, but extend out to a radius of $50''$. We then combined the synthetic profiles with the bright star profiles to create PSF images in each band that include the effects of scattered light both at small and large radii. The synthetic, bright star and combined PSF i-band profiles are shown in Figure 3 along with the stack light profile. In the Appendix, we perform additional testing of the effects of different PSF models on our results.

3.2. PSF Deconvolution and Surface Brightness Profiles

Several techniques have been proposed and widely used for PSF deconvolution from imaging data (e.g., Lucy 1974; Högbom 1974). These algorithms, however, typically work well either in the inner parts of galaxies or their faint outskirts but not both simultaneously. We therefore chose to use the recently introduced technique of Szomoru et al. (2010) for PSF deconvolution from our LRG stacks. Following this method, we first used GALFIT 3.0 (Peng et al. 2002) to fit a two-dimensional Sérsic model with the combined PSF images serving as the input convolution kernel. For the purpose of pixel weighting, to which the GALFIT results are sensitive, we supplied the software with the weight masks produced for each stack (Section 2.3). We then constructed a synthetic Sérsic profile from the best-fit parameters to which we added the residuals that were left

[1] http://www.sdss.org/dr7/products/images/read_psf.html

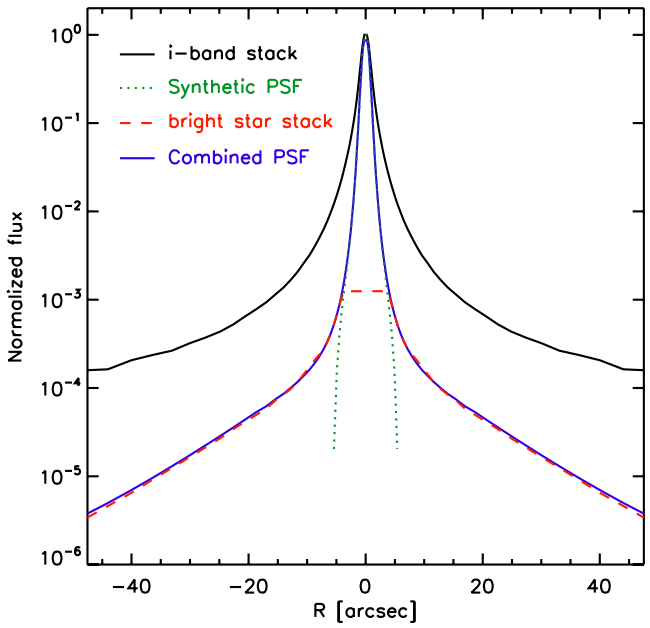

Figure 3. Radial light profile of the *i*-band stack (black solid line) overlaid with light profiles of the synthetic PSF stack (green dotted line), the bright star PSF stack (red dashed line), and the combined PSF (solid blue line). Light scatter due to the PSF is most significant in *i*-band images.

(A color version of this figure is available in the online journal.)

after subtracting the PSF convolved model from the image. In their paper, Szomoru et al. (2010) showed that this method is insensitive to variations in the Sérsic parameters used to create the model. In order to increase the flexibility of our model fits, we left the background level as a free parameter, in effect fitting the light profiles with a simple two-component model of a constant plus a Sérsic function. We also ran GALFIT with the background level set to zero in order to test how the lack of a constant component affects the model fits. Finally, we measured the total flux in the light profile before and after deconvolving the PSF from it in order to verify that flux is globally conserved. We found that the difference between the total flux within the analysis radius of 475 kpc is less than 0.5% between the deconvolved and the original profiles.

Figure 4 shows the PSF-deconvolved profile of the *r*-band stack (the stack of galaxy images in the *r* band) along with the GALFIT Sérsic model fit. To derive the profiles, we first applied the IRAF task *ellipse* on the average of the *r*, *i*, and *z* stacks while allowing the central position, ellipticity, and position angle to vary with radius. We then used the output table from this fit as an input template for obtaining the light profiles of the stacks and models. The error bars were derived using randomly selected field stacks (see Section 3.3 for details). Also shown in the figure are the initial *r*-band profile and the residual background level as determined by GALFIT.

We note that an ideal deconvolution of the light profile would require a radially varying PSF which is weighted by the number of galaxies stacked in each radius bin. However, we assume that this would have a negligible effect on the properties of the light profiles compared to other systematic effects and do not further modify the image PSF deconvolution.

3.3. Profile Error Analysis

The unprecedented depth and background uniformity of the stacks reveal faint emission hundreds of times dimmer than the typical LRG central surface brightness. In images of such low level emission statistical errors are not the only significant, and perhaps not even the main, source of noise. Errors in the faint outskirts of the stacks from undetected sources and remaining flattening issues and their effect on the model fits become increasingly important but also increasingly hard to assess. We therefore used the same random stacks that are described in Section 2.4 to measure the effects of such biases on the stack light profile properties. We subtracted each random background image from its corresponding magnitude-bin stack and created 100 stacks per filter, repeating the steps described in Sections 2.3 and 2.5. We then followed the procedure described in Section 3.2 to deconvolve the PSF from the stacks and derived a Sérsic parameter set for each random stack. Table 1 shows that the scatter around the obtained Sérsic values due to these errors is small, suggesting that the fit is weighted toward the luminous inner part of the stacks. The Sérsic index 1σ deviations of all but the faint *u*-band stack are under 0.1 and the effective radius 1σ deviations are under 0.2 kpc. In addition, we used the IRAF task *ellipse* to obtain radial light profiles for each of the random background-subtracted stacks, using the same input template table as was used in Section 3.2. The error bars in Figures 4, 6, and 8 reflect the 1σ scatter of surface brightness profile fits to the random stacks.

Table 1
Stack Sérsic Parameters

Filter	Sérsic Index	Effective Radius (kpc)
u	3.94 ± 1.62	17.0 ± 9.80
g	4.03 ± 0.09	12.6 ± 0.19
r	5.50 ± 0.05	13.1 ± 0.10
i	4.86 ± 0.05	10.9 ± 0.06
z	4.91 ± 0.08	11.5 ± 0.12

Systematic errors in the measured profiles that may rise from stacking images of galaxies with a range of Sérsic parameters seem to be of lesser significance. van Dokkum et al. (2010, Appendix B) stacked hundreds of synthetic model images with randomly generated Sérsic profiles and showed that the stack effective radius and Sérsic index *n* match well with the average values of the stacked profiles. This suggests that no additional significant errors are introduced by our stacking technique.

3.4. Undetected Light Correction

Despite aggressive masking of foreground and background objects prior to stacking the data some light from undetected, and therefore unmasked, sources remains in the images. In order to correct the stack light profiles for this effect, we used the LRG images to derive an empirical luminosity function for the LRG group environment at $z \sim 0.34$. We started by using SExtractor to extract photometry for all the objects in the LRG frames using the detection limits that were used for object masking. We then binned the resultant values with a bin size of 0.01 dex in log space and produced a luminosity function (in practice we produced an observed brightness function). We repeated both steps for an identical number of randomly selected fields from the same SDSS imaging fields and produced a luminosity function for background and foreground sources. The LRG group luminosity function is then given by the difference between the number of sources in a particular brightness bin in the LRG fields and the number of random field sources in the same brightness bin (see Figure 5).

The contribution of light from undetected objects to the stack profile comes from the faintest group members whose

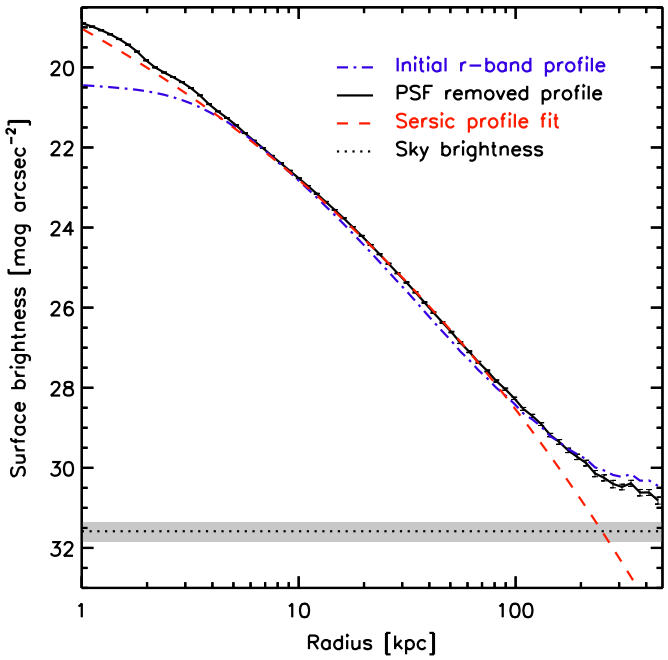

Figure 4. PSF-deconvolved profile of the r-band stack (black solid line) is shown along with the best GALFIT Sérsic model (red dashed line). The sky brightness level as determined by GALFIT is also plotted (black dotted line), along with the 1σ variation in the random stack measurements. The error bars are the standard deviation of a distribution of 100 model fits using randomly selected stacked fields (see Section 3.3 for details). This profile is corrected for undetected group galaxies using the empirical luminosity function described in Section 3.4.

(A color version of this figure is available in the online journal.)

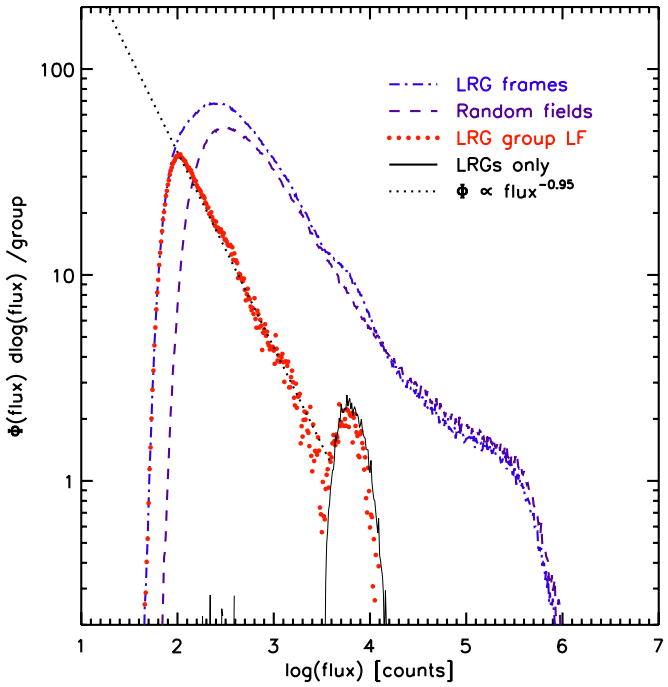

Figure 5. Empirical LRG group luminosity function (thick red dots) was derived by subtracting the luminosity function of objects in randomly selected frames (purple dashed line) from that of the LRG frames (blue dot-dashed line). The LRG only luminosity function is also plotted, along with the best-fit power-law curve to the faint-end slope.

(A color version of this figure is available in the online journal.)

luminosity function is expected to be well fitted by a power-law function. We therefore divided the LRG group luminosity function into an LRG component and a power-law component (solid and dotted black curves in Figure 5). The best-fit power-law curve to the data is relatively shallow, with a slope of $\Phi \propto \mathrm{flux}^{-0.95}$, implying that less than 0.3% of the total unmasked light in the group (the total light in LRGs and undetected objects) comes from undetected sources.

Finally, we extracted a radial light profile from the flux of resolved (and masked) objects in the LRG frames and fitted it with a single parameter Sérsic model. We then normalized the best-fit curve such that the total flux under it equaled 0.3% of the total LRG flux. Assuming that the radial light distribution of the unresolved sources is identical to that of the resolved objects, we subtracted the resultant correction profile from the stack light profile. This correction did not change the LRG profile significantly and only moved it within the error bars for any given radius bin.

3.5. Sérsic Profile Fits

The derived profiles of the g-, r-, i-, and z-band stacks are well fitted by a single Sérsic parameter set out to $r = 100$ kpc, at which radius the profiles deviate from the model by 0.2 mag arcsec^{-2}, corresponding to a difference of roughly 20%. This is shown in Figure 6, where the PSF-deconvolved profiles of all five stacks are plotted along with their best GALFIT models. The determined Sérsic index values for the u- and g-band profiles are $n \sim 4$ and are slightly shallower than those of the redder colors with $n \sim 5$ for the r-, i-, and z-band stacks. The effective radii of all profiles except for the u-band stack are between 11 and 13 kpc with errors under 0.2 kpc. As might have been expected, setting the background level to zero in GALFIT increased the best-fit effective radii and Sérsic parameters by up to 10% as GALFIT attempted to fit the excess light at large radii. At radii larger than 100 kpc, the profiles deviate from the model and excess light is observed in the g-, r-, i-, and z-band stacks. Figure 6 also shows that at $r > 200$ kpc there is 30%–70% more light in the PSF-deconvolved profiles than in their respective best-fit models.

The derived profile parameters for the five final stacks are presented in Table 1.

3.6. Rotated LRG Stacks

Early work in the field of massive galaxy evolution showed that the average ellipticity of nearby ellipticals is $0.3 < \epsilon < 0.4$, with a smaller value for the most massive systems (e.g., Sandage et al. 1970; Binney & de Vaucouleurs 1981). The average ellipticity of LRGs can be measured from our image stacks. We used SExtractor to derive a position angle for each of the 42,579 galaxies, rotated all frames to a common axis and stacked them following the steps described in Section 2. We then deconvolved the PSF from the stacks using the technique discussed in Section 3.2. Since this technique utilizes Sérsic parameter fits with radially constant ellipticities as the underlying model, we tested our results by deconvolving the r-band stack using the Lucy (1974) algorithm. Figure 7 shows the rotated stack ellipticities in four of the bands, excluding the u-band stack due to its significantly noisier profile (as can be seen in Figure 6). Also plotted are the original, not PSF-deconvolved r-band stack (black dashed line) and the Lucy-deconvolved r-stack profile (purple dot-dashed line). All profiles were obtained using the IRAF task *ellipse* and all are flat out to roughly 60 kpc with an average ellipticity value of 0.26 between 10 and 60 kpc

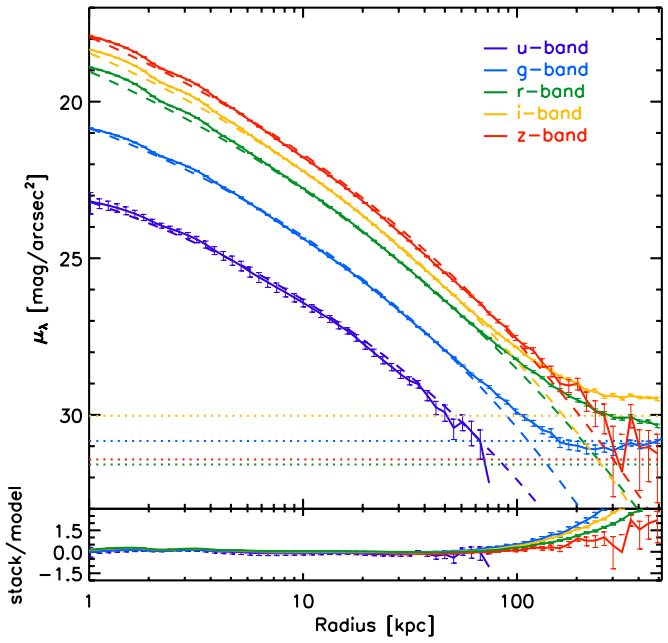

Figure 6. Light profiles of the five stacks are plotted along with their best-fit model and the residual sky background as determined by GALFIT. The quotients of each model and light profile pair are also plotted, showing good agreement out to 100 kpc. The error bars are the standard deviation of a distribution of 100 model fits using randomly selected stacked fields (see Section 3.3 for details).

(A color version of this figure is available in the online journal.)

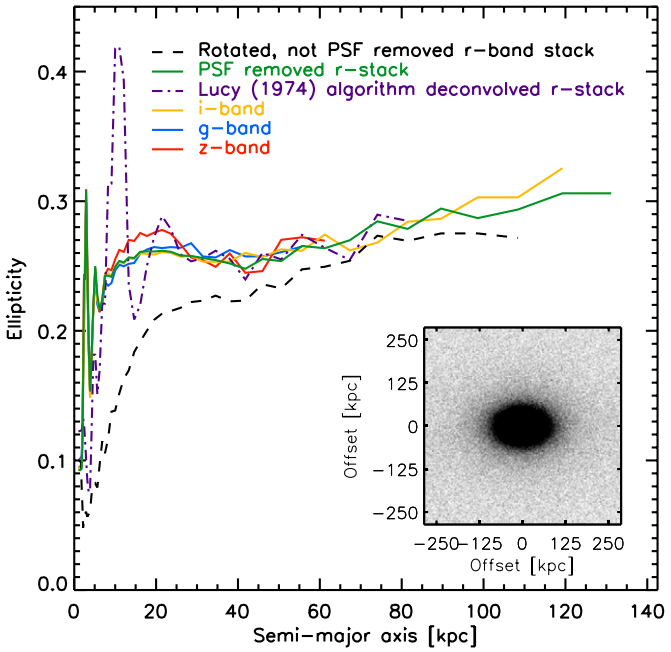

Figure 7. Ellipticity of the rotated stacks as a function of radius. The solid curves represent the profiles of the PSF-deconvolved stacks in the r, i, g, and z bands. The ellipticity in all filters is relatively flat out to roughly 60 kpc, where a mild rise is observed. The initial r-band stack profile (black dashed line) and the Lucy (1974) deconvolved profile (purple dot-dashed line) are also shown. The bottom-right inset shows the r-band rotated stack.

(A color version of this figure is available in the online journal.)

($\epsilon = 0.21$ when the centers are not excluded). The radial dependence of the ellipticity outside of 60 kpc appears to be mild, with a slight rise to $\epsilon \sim 0.3$ at $r = 100$ kpc. Furthermore, the profiles of both PSF-deconvolved and PSF-deconvolved stacks are in good agreement with each other, with less scatter in the inner parts of the former. From a similarly rotated stack of brightest cluster galaxy (BCG) images, Zibetti et al. (2005) found a steep rise in profile ellipticity outside of roughly 80 kpc followed by a steep decline at radii greater than 200 kpc. In the range 80–200 kpc, this trend is similar to what we observe for LRGs, suggesting that there may be a continuum of properties going from group to cluster environments. We note that Zibetti et al. (2005) did not correct their stacks for PSF-induced effects.

3.7. Color Gradients

It has long been known that the broadband colors of nearby elliptical galaxies vary with radius in the optical regime (Vader et al. 1988; Franx et al. 1989; Peletier et al. 1990). Nevertheless, studies measuring such color gradients typically rely on observations of the inner parts of these objects, out to only 2–3 effective radii. In Figure 8, we plot the color profiles of $r - i$ and $g - z$. The color pairs (r and i, g and z) have similar ellipticity profile sizes to ensure that the stack depths are comparable (Figure 7). We compare our results with a study of nearby ellipticals by Peletier et al. (1990) and show that the profile shapes of the two studies agree well out to a radius of ∼30 kpc. The stack color values are plotted in the observed frame and are matched to the Peletier et al. (1990) rest-frame colors by adding a constant. We note that outside of about 20 kpc the local sample is composed of only a few galaxies where sufficient depth was achievable. With the advantage of our deep stacks, however, we are able to study the colors of LRGs out to more than eight effective radii. This is the first time that the colors of massive galaxies are observed at such large radius, providing a new insight on the stars that are found in the outskirts of massive galaxies. Indeed, the color profiles of LRGs change trend beyond the limit of nearby galaxy observations. Despite initially getting bluer in the inner 40 kpc of both plotted colors, the profiles quickly flatten out to a relatively constant value. The outskirts of LRGs are then roughly 0.15 dex and 0.2 dex bluer than their centers in the $r - i$ and $g - z$ colors, respectively.

The color profile is different from that observed by Z05 at $r > 20$ kpc as Z05 find that BCGs become very red at large radii. As we show in the Appendix, the Z05 color profile may be severely affected by PSF effects at all radii, including the stack outer parts. Therefore, the different radial color profiles do not necessarily imply that LRGs and BCGs are fundamentally different objects. We note that the $g - r$ color gradient found by Z05 has a similar slope as the $g - z$ profile presented in Figure 8. The $g - r$ profile of Z05 may suffer less from PSF effects than their $r - i$ profile.

4. DISCUSSION

4.1. Light Profiles and the Size of Massive Galaxies

The first and foremost result that arises from this study is that faint, gravitationally bound stellar light can be traced in massive elliptical galaxies out to a radius of 100 kpc. By stacking a large number of faint galaxy images, we detect light at such distance from the centers of massive galaxies with good confidence. In Figure 10, we show that the total accumulated light at $20 < r/\mathrm{kpc} < 100$ is non-negligible and accounts for roughly 27% of the overall flux in the stack. In fact, more than 13% of the stack light can be detected at very large radii outside of $r = 100$ kpc or more than eight effective radii. This is especially interesting in light of recent studies that find compact massive galaxies at $z \sim 2$, exhibiting effective radii of only 1 kpc (e.g.,

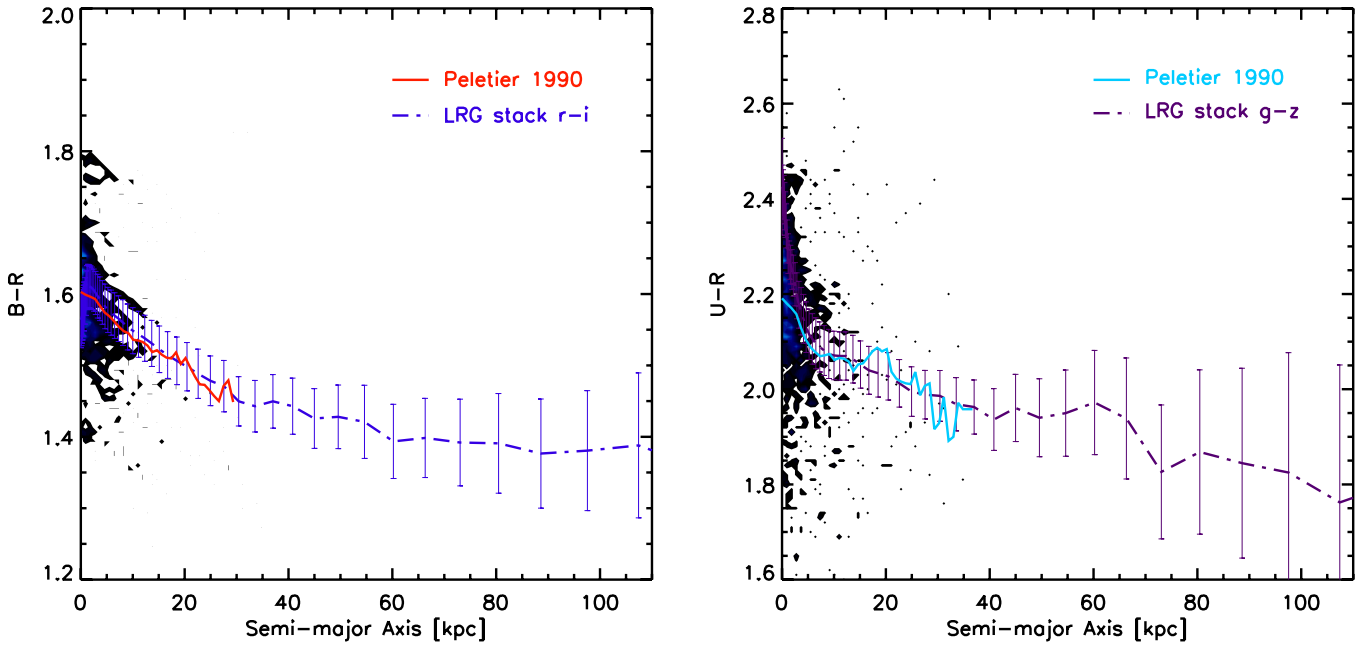

Figure 8. Broadband color comparison between the inner parts of nearby galaxies from Peletier et al. (1990) and the stacks. The blue density plots show the distribution of nearby galaxy colors out to about three effective radii and the red and light blue solid lines follow the running means of the sample. The blue and purple dot-dashed lines represent the $r - i$ and $g - z$ colors of the stacks, respectively, which match well with the Peletier et al. (1990) color profiles. Both colors are flat, within the error bars, outside of about 40 kpc.

(A color version of this figure is available in the online journal.)

Daddi et al. 2005; Trujillo et al. 2006; van Dokkum et al. 2008). The size growth of these objects is evidently rapid, expanding the physical scale of the galaxy by a factor of at least five in less than 10 Gyr. Unfortunately, the physical growth mechanism cannot be directly observed in the LRG stacks as any signal from individual galaxies is smoothed and averaged over the entire sample. Nevertheless, the lack of a clear change in the stack light profile slopes out to 100 kpc suggests that the observed light in the outskirts of LRGs is physically associated with the galaxies and their inner parts. Further evidence for this comes from the relatively radially independent ellipticity profiles which vary only slightly out to 100 kpc. Any other light sources, such as background contamination or residual PSF scattering, would be uncorrelated with the position angle of the LRG as measured in individual SDSS images, resulting in a circular light distribution.

Outside of roughly 100 kpc, the light profiles of the g-, r-, i-, and z-band stacks depart from the simple Sérsic model profile and exhibit excess light (Figure 6). This departure from a simple model is observed here for the first time in LRGs and it shows that stars at the extreme outskirts of massive galaxies follow a different gravitational potential than stars in the inner parts. It is known that the potential at these radii is dominated by the properties of the dark matter halo, implying that the light profile is not necessarily expected to follow the same model that describes the inner stellar body. Alternatively, this excess light may simply be the residual background in the images, reflecting unresolved light from the group environment in which LRGs typically reside.

Excess light was also observed by Z05, who studied the ICL around the brightest cluster galaxies from a stack of 683 SDSS images. Such galaxies typically live in dense halos with total mass of 10^{14}–10^{15} $M_{\odot}$ and are inherently different from LRGs whose group halos are a few times 10^{13} $M_{\odot}$ in mass. Z05 found that in clusters this "extra light" constitutes only a small fraction of the total cluster profile, accounting for less than 11% of the light inside of 500 kpc. Nevertheless, the ICL profile departs from a single parameter Sérsic model already at $r \sim 50$ kpc, compared to the departure radius of 100 kpc that is observed in our LRG stacks (Figure 9). This suggests that the massive clusters studied by Z05 may more readily support a population of intergalactic stars than the groups in which LRGs reside. In their paper, Z05 correct their light profiles for unresolved cluster sources using the luminosity function given by Mobasher et al. (2003). We note that the PSF, which is not deconvolved from the ICL+BCG profiles presented in Z05, may scatter light at all radii and increase the errors of the Sérsic model fit.

Unlike the outer parts of LRGs, the centers of these galaxies are not well resolved in our stacks. Studies utilizing high-resolution *Hubble Space Telescope* (*HST*) images showed that the profile at the inner parts of nearby ellipticals often departs from the Sérsic model that traces their outskirts. More specifically, the most massive ellipticals exhibit flattened central light profiles (e.g., Lauer 1985; Kormendy et al. 1994; Lauer et al. 1995; Faber et al. 1997; Graham et al. 2003). Recently, Kormendy et al. (2009) used a compilation of *HST* and ground-based data to show that although well fitted by a Sérsic model out to large radii, the most massive Virgo ellipticals exhibit 1 kpc scale cores. In our stacks, we cannot resolve such physical scales as 1 pixel in the SDSS data is equivalent to 1.9 kpc at the stack mean redshift of 0.34. We are nevertheless able to confirm the excellent fit of massive elliptical galaxy profiles to a single Sérsic profile out to a few effective radii that Kormendy et al. (2009) found for individual Virgo galaxies (reaching $\Delta\mu_{\lambda} \geqslant 0.2$ mag arcsec^2 at $r_{\lambda} \geqslant 100$ kpc).

4.2. How Much Light is Missed?

The deep stacks allow us to test how much light is missed in typical studies of the profiles of individual LRGs and derive a correction factor that can be applied in such cases. To do

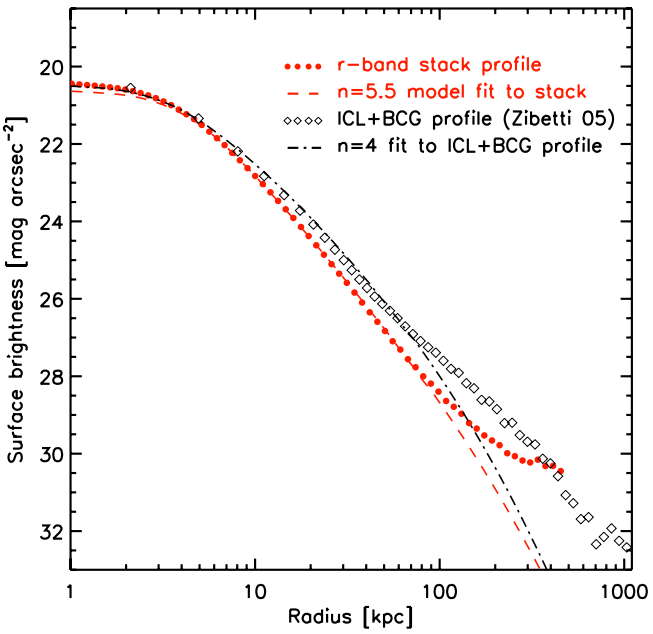

Figure 9. Comparison between the light profiles of our LRG *r*-band stack and the ICL profile from Zibetti et al. (2005). The ICL profile departs from a single parameter Sérsic model at 50 kpc, or double the departure radius of 100 kpc that is observed in the LRG stack. This suggests a more significant population of intergalactic stars in massive clusters than in groups.

(A color version of this figure is available in the online journal.)

so we first selected all the LRGs in a single magnitude bin, $18.0 \leqslant m_r < 18.2$, and used GALFIT to produce a Sérsic model to each object individually. We then excluded all fits with errors of more than 10% in either the n parameter or the effective radius, resulting in a mean effective radius value of 11.7 kpc. The difference between this value and the one derived by GALFIT for the stacked image ($r_e = 13.1$ kpc) is then ∼10%. This implies that surveys may underestimate the size of massive red galaxies by this amount. The total flux in the stack, however, accounts for ∼20% more than the mean value for the individually derived profiles, suggesting that a non-negligible amount of light is typically missed and that the total stellar mass is underestimated.

4.3. Minor Mergers and the LRG Color Profile

It has long been known that the color profiles of nearby massive ellipticals exhibit a relatively smooth gradient toward bluer colors from the galaxy centers outward. Line index measurements (e.g., Carollo et al. 1993; Davies et al. 1993; Spolaor et al. 2010) and studies of high-redshift galaxies (Tamura et al. 2000) provide evidence that this observed color gradient originates from a radial slope in stellar metallicity. It has also been claimed in these studies that age plays only a secondary role in producing this trend. Nevertheless, it is yet to be determined which physical mechanisms create and evolve the observed color gradient. With the color profile in mind, we will discuss in this section a previously suggested model in which minor mergers and low mass accretion events are the main supplier of stars to the outskirts of massive galaxies. We will also utilize our LRG stacks to provide additional pieces of evidence that support this model.

4.3.1. Creating the Faint Stellar Halo

It has been suggested that the size and mass growth of massive galaxies are dominated by minor mergers which contribute a relatively constant flow of accreted mass over a long time. This is evident from analytic calculations (e.g., Bezanson et al. 2009), numerical simulations of large volumes (e.g., Lucia & Blaizot 2007; Naab et al. 2007), and observations of nearby elliptical galaxies (e.g., van Dokkum 2005; Tal et al. 2009). The contribution of accreted mass, however, is not expected to be uniform throughout the galaxy. This can be shown using very simple energy arguments following the assumption that accreted mass is more likely to stay near the radius at which it was accreted if its total energy budget is similar to the gravitational energy of the accreting galaxy at that radius. In other words, if the escape velocity of a star in an infalling galaxy equals the orbital velocity of the accreting galaxy at the radius at which the star escapes, this star will likely fall into orbits close to that radius. If on the other hand the star escapes the infalling galaxy at any other radius, it will either fall closer to or be thrown farther from the center of the accreting galaxy, thus contributing to a more uniform mass distribution. This argument can be described by the following equation:

$$V_{\rm circ}^{M} = V_{\rm esc}^{m}, \tag{1}$$

where $V_{\rm circ}^{M}$ is the circular velocity of the accreting galaxy and $V_{\rm esc}^{m}$ is the escape velocity from the infalling galaxy. This can be expressed in terms of the masses of the accreting and infalling galaxies, M and m are the accretion and escape radii, R_a and r,

$$R_a = \frac{M}{m}\frac{r}{2}. \tag{2}$$

Equation (2) implies that more massive infalling galaxies will preferentially deploy most of their stars closer to the center of the accreting galaxy. However, the mass ratio M/m cannot be close to 1 since such major mergers will violently disrupt both galaxies and not simply disperse the stars of one into the stellar body of the other. In addition, if the mass ratio is high, the contribution of the infalling galaxy to the colors of the accreting galaxy will be minor. We therefore assume typical values of $4 < M/m < 10$ for the mass ratio and $2 < r/\mathrm{kpc} < 10$ for the escape radius, both roughly correspond to the accretion of an $L^{\star}$-type galaxy. It is therefore convenient to re-write Equation (2) using the suggested average values for M/m and r:

$$R = 42\left(\frac{M/m}{7}\right)\left(\frac{r}{6\,\mathrm{kpc}}\right)\mathrm{kpc}. \tag{3}$$

This simple model provides a possible explanation for the observed size growth from $z = 2$, as well as the smooth gradient and flattening in the stack color profile. It enables infalling low mass galaxies to easily deploy the majority of their stars outside of the accretion radius R_a and it suggests that scattered stars that are stripped from their galaxy at any other radius may end up close to the center. This may be the case if the accreting galaxy is indeed red and if a significant part of all infalling galaxies are bluer than the LRG. In addition, this scenario supports minor mergers with large M/m values as the main size growth mechanism as stars are preferentially being deployed far from the center of the accreting galaxy without increasing its total mass significantly.

4.3.2. The Frequency of Minor Mergers

The frequency of low mass accretion events is a critical factor in assessing the importance of these interactions to the size and mass growth of massive ellipticals. Minor mergers must not be

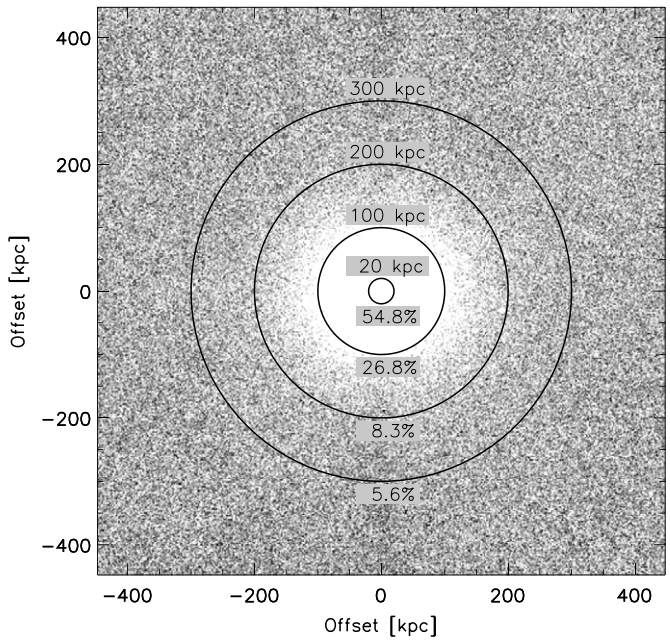

Figure 10. Radial stellar light fraction of the *r*-band stack in four radius bins of 20, 100, 200, and 300 kpc. Note that a non-negligible fraction of the light is detected in the extreme outskirts of the stack.

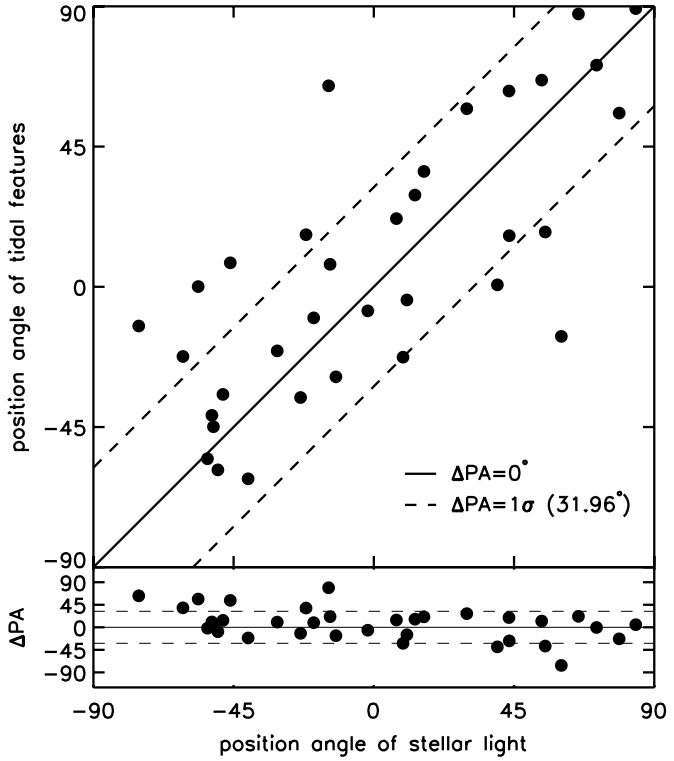

Figure 11. Comparison between the position angle of stellar light and that of tidal feature light in galaxies from the OBEY survey (Tal et al. 2009). The correlation between the orientation of tidal features and the stellar body suggests that minor interactions cannot be ruled out as a source of stellar light to the outskirts of massive galaxies.

rare in order for the compact galaxy at $z = 2$ to experience the observed rapid size growth. We now also know that the light at $r > 20$ kpc comprises roughly 40% of the total stellar light (Figure 10), suggesting that a constant stream of accreted mass is required. This implied mass growth confirms the results from van Dokkum et al. (2010) who found that nearby ellipticals are roughly twice as massive as compact $z = 2$ galaxies.

Observations of early-type galaxies reveal ample evidence for close gravitational interactions between ellipticals and their neighboring galaxies. Such interactions, mainly in the form of minor mergers, leave their signature on the stellar bodies of the massive galaxy for a time period that depends on the interaction itself and that can last for up to a few Gyrs. Initial attempts to characterize tidal features around nearby ellipticals relied heavily on qualitative descriptions of the remnant morphology but nevertheless revealed evidence for interaction in many systems (Schweizer & Seitzer 1992). More recent studies quantified an interaction parameter by measuring excess light in the tidal features compared to smooth models of the systems. Such studies analyzed volume-limited samples of nearby galaxies, finding that more than 70% of all ellipticals have had one or more recent minor merger events (van Dokkum 2005; Tal et al. 2009). The mass growth that is inferred from this high interaction rate can be estimated at a factor of 2–3 since $z = 2$ (see Tal et al. 2009 for details).

4.3.3. Minor Mergers and the Ellipticity Profile

Assuming that the distribution of infalling galaxies and therefore also tidal features is spherically symmetric around the elliptical, the stack outskirts are expected to be relatively round, in apparent conflict with the trend shown in Figure 7. It is however possible that gravitational interactions contribute to the ellipticity of the host galaxy or alternatively occur preferentially along the major axis of the dark matter halo, thus aligning the resultant tidal features with the position angle of the elliptical. In order to test this, we examined galaxies from the OBEY survey (Tal et al. 2009), a complete sample of nearby ellipticals that was utilized to study and quantify tidal features in the stellar bodies of these objects. We measured the overall ellipticity of each galaxy with a tidal parameter value of at least 0.07 and compared it to the second moment of light distribution in the model-subtracted residual image. By measuring the second moment of residual light distribution, we quantified, in effect, the position angle of tidal features. Figure 11 shows that a correlation indeed exists between the orientation of the stellar body and that of the tidal features. A Spearman's rank test finds that the probability that this correlation was drawn from a random distribution is less than 0.1%. We also note that only two galaxies exhibit ΔP.A. $> 60^\circ$. Although such a suggestive correlation does not strongly support any single scenario as the main mechanism for creating the observed faint halos, its existence hints that minor mergers at least cannot be ruled out as a significant contributor to the stellar bodies of LRGs at large radii.

This analysis is therefore consistent with the idea that minor mergers and gravitational interactions likely play an important role in determining the properties of massive red galaxies. Foremost is the blue color index of the profile at $r > 40$ kpc which suggests that the outer halo is composed of younger or alternatively more metal-poor stars compared to the center. This probably means that the stellar populations of the outskirts were formed separately from those in the center and probably accreted at a later time. This scenario is supported by the observed high rate of tidal features around nearby elliptical galaxies, although we note that the LRGs are typically more massive by a factor of $\gtrsim$2 than the galaxies in the Tal et al. (2009) sample. Our analysis shows that such accretion events likely deploy most of the stars at large radii.

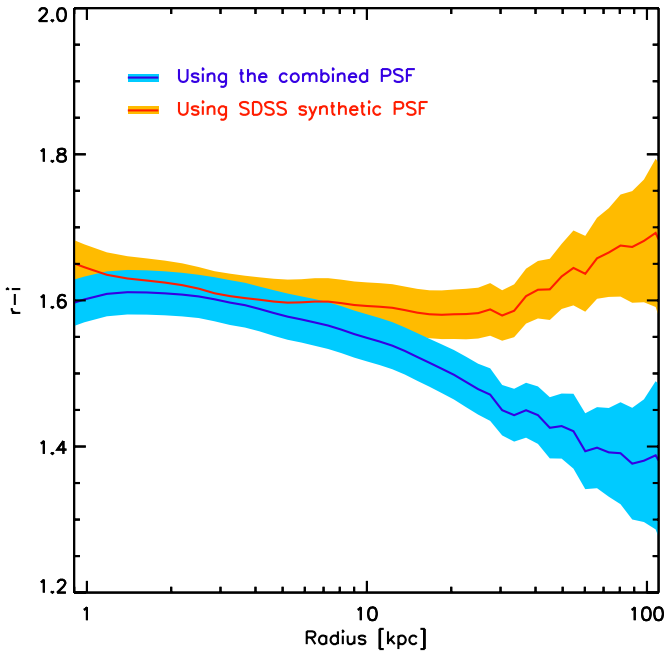

Figure 12. Color profile comparison between the combined PSF-deconvolved stack (blue line) and the synthetic only PSF-deconvolved stack (red line). The shaded areas show the 1σ error bars derived using randomly selected field stacks (Section 3.3). The use of insufficiently sampled PSF profile artificially creates an red halo in our stacks.

(A color version of this figure is available in the online journal.)

5. SUMMARY AND CONCLUSIONS

In this paper, we stacked more than 42,000 images of LRGs in order to study the faint light of these objects at large radii. In our stacks, we detected stellar light out to radii greater than 100 kpc, thus providing a correction factor to the true size and overall stellar mass of LRGs. This is the first time that such an analysis is performed using a data set of this scale, reaching unprecedented depth for $z > 0.01$ galaxies. The relatively flat ellipticity profile (Figure 7) verifies that the light detected at large radii is physically associated with the stellar body. Interestingly, the profiles suggest increased ellipticity at large radii of the average LRG profile.

In agreement with Kormendy et al. (2009), we confirmed that, on average, the light profiles of massive ellipticals can be well described by a single Sérsic model out to roughly eight effective radii. Outside of 100 kpc, the profiles deviate from a simple Sérsic model and exhibit extra light in the r-, i-, and z-band stacks. This excess light can probably be attributed to unresolved intragroup light or a change in the light profile itself. Differentiating between these possibilities, however, may be difficult as both can have a similar effect on the profile shape at large radii.

Finally, we utilized the five optical bands of SDSS to study the colors of these galaxies and showed that the well-known decrease in color index out to 2–3 effective radii flattens out and stays blue compared to the galactic centers out to the detected stack limit. Although this finding by itself does not favor any one stellar population evolution scenario, it suggests that the central 20 kpc evolve somewhat differently from the rest of the galaxy. Previous studies of line indices in early-type galaxies suggest that this difference can probably be attributed to a difference in metallicity.

We are grateful to Marijn Franx for many useful comments and to David Wake and Adam Muzzin for numerous engaging discussions. We also thank Stefano Zibetti for sharing his ICL light profiles with us.

Funding for the SDSS and SDSS-II was provided by the Alfred P. Sloan Foundation, the Participating Institutions, the National Science Foundation, the US Department of Energy, the National Aeronautics and Space Administration, the Japanese Monbukagakusho, the Max Planck Society, and the Higher Education Funding Council for England. The SDSS was managed by the Astrophysical Research Consortium for the Participating Institutions.

Funding for the SDSS and SDSS-II has been provided by the Alfred P. Sloan Foundation, the Participating Institutions, the National Science Foundation, the US Department of Energy, the National Aeronautics and Space Administration, the Japanese Monbukagakusho, the Max Planck Society, and the Higher Education Funding Council for England. The SDSS Web site is http://www.sdss.org/.

The SDSS is managed by the Astrophysical Research Consortium for the Participating Institutions. The Participating Institutions are the American Museum of Natural History, Astrophysical Institute Potsdam, University of Basel, University of Cambridge, Case Western Reserve University, University of Chicago, Drexel University, Fermilab, the Institute for Advanced Study, the Japan Participation Group, Johns Hopkins University, the Joint Institute for Nuclear Astrophysics, the Kavli Institute for Particle Astrophysics and Cosmology, the Korean Scientist Group, the Chinese Academy of Sciences (LAMOST), Los Alamos National Laboratory, the Max-Planck-Institute for Astronomy (MPIA), the Max-Planck-Institute for Astrophysics (MPA), New Mexico State University, Ohio State University, University of Pittsburgh, University of Portsmouth, Princeton University, the United States Naval Observatory, and the University of Washington.

APPENDIX

THE WINGS OF THE PSF PROFILE

Light scattered by the wings of the PSF profile was shown to contribute noticeably to the color profiles of the outskirts of spiral galaxies. In his paper, de Jong (2008) argues that the choice of PSF model used for image deconvolution is crucial for analyzing data of spiral galaxies. The author further claims that the red stellar halos found by previous studies were artificially produced by PSF models that were poorly sampled at large radii. In this Appendix, we confirm this observation and show that the widely used synthetic PSF images may lead to inaccurate color gradients even in the peaky light profiles of massive red galaxies.

In order to test the effects of PSF profile selection on the properties of the derived Sérsic model, we followed the procedure described in Section 3.2 to deconvolve the stacks using two different PSF images in each observed band. The first profile is identical to the one used throughout this study and it combines a synthetically produced PSF model with a bright star stack (Section 3.1), while the second utilizes only the synthetic PSF image produced by the Read Atlas Image code. While the u, g, r, and z models are less than 15% larger when using only the synthetic PSF image, the i-band stack exhibits an increase of more than 25% in this case. The increased growth in model size in the i band compared to the other stacks implies that the halo of these galaxies may erroneously appear to be red. This is most clearly evident in Figure 12, where we plot the $r - i$ color

profiles of the two PSF-deconvolved models and show that in the synthetic only case an artificial red halo appears outside of roughly 40 kpc. We conclude, in agreement with de Jong (2008), that a proper choice of a well-sampled PSF model is critical for studying the faint outskirts of galaxies.

REFERENCES

Abazajian, K. N., et al. 2009, ApJS, 182, 543
Bergvall, N., Zackrisson, E., & Caldwell, B. 2010, MNRAS, 405, 2697
Bertin, E., & Arnouts, S. 1996, A&AS, 117, 393
Bezanson, R., van Dokkum, P. G., Tal, T., Marchesini, D., Kriek, M., Franx, M., & Coppi, P. 2009, ApJ, 697, 1290
Binney, J., & de Vaucouleurs, G. 1981, MNRAS, 194, 679
Boroson, T. A., Thompson, I. B., & Shectman, S. A. 1983, AJ, 88, 1707
Caon, N., Capaccioli, M., & Rampazzo, R. 1990, A&AS, 86, 429
Carollo, C. M., Danziger, I. J., & Buson, L. 1993, MNRAS, 265, 553
Daddi, E., et al. 2005, ApJ, 626, 680
Davies, R. L., Sadler, E. M., & Peletier, R. F. 1993, MNRAS, 262, 650
de Jong, R. S. 2008, MNRAS, 388, 1521
Dressler, A., Lynden-Bell, D., Burstein, D., Davies, R. L., Faber, S. M., Terlevich, R., & Wegner, G. 1987, ApJ, 313, 42
Eisenstein, D. J., et al. 2001, AJ, 122, 2267
Faber, S. M., & Jackson, R. E. 1976, ApJ, 204, 668
Faber, S. M., et al. 1997, AJ, 114, 1771
Franx, M., Illingworth, G., & Heckman, T. 1989, AJ, 98, 538
Gonzalez, A. H., Zabludoff, A. I., Zaritsky, D., & Dalcanton, J. J. 2000, ApJ, 536, 561
Graham, A. W., Erwin, P., Trujillo, I., & Asensio Ramos, A. 2003, AJ, 125, 2951
Högbom, J. A. 1974, A&AS, 15, 417
Illingworth, G. 1977, ApJ, 218, L43
Kormendy, J., & Djorgovski, S. 1989, ARA&A, 27, 235
Kormendy, J., Dressler, A., Byun, Y. I., Faber, S. M., Grillmair, C., Lauer, T. R., Richstone, D., & Tremaine, S. 1994, in ESO Conference and Workshop Proceedings 49, Dwarf Galaxies, ed. G. Meylan & P. Prugniel (Garching: ESO), 147
Kormendy, J., Fisher, D. B., Cornell, M. E., & Bender, R. 2009, ApJS, 182, 216
Krick, J. E., & Bernstein, R. A. 2007, AJ, 134, 466
Lauer, T. R. 1985, ApJ, 292, 104
Lauer, T. R., et al. 1995, AJ, 110, 2622
Loeb, A., & Peebles, P. J. E. 2003, ApJ, 589, 29
Lucia, G. D., & Blaizot, J. 2007, MNRAS, 375, 2
Lucy, L. B. 1974, AJ, 79, 745
Mihos, J. C., Harding, P., Feldmeier, J., & Morrison, H. 2005, ApJ, 631, L41
Mobasher, B., et al. 2003, ApJ, 587, 605
Naab, T., Johansson, P. H., Ostriker, J. P., & Efstathiou, G. 2007, ApJ, 658, 710
Peletier, R. F. 1989, Elliptical Galaxies-Structure and Stellar Content, http://adsabs.harvard.edu/abs/1989PhDT.....149P
Peletier, R. F., Davies, R. L., Illingworth, G. D., Davis, L. E., & Cawson, M. 1990, AJ, 100, 1091
Peng, C. Y., Ho, L. C., Impey, C. D., & Rix, H. 2002, AJ, 124, 266
Reid, B. A., & Spergel, D. N. 2009, ApJ, 698, 143
Sandage, A., Freeman, K. C., & Stokes, N. R. 1970, ApJ, 160, 831
Schweizer, F., & Seitzer, P. 1992, AJ, 104, 1039
Spolaor, M., Kobayashi, C., Forbes, D. A., Couch, W. J., & Hau, G. K. T. 2010, MNRAS, 408, 272
Szomoru, D., et al. 2010, ApJ, 714, L244
Tal, T., van Dokkum, P. G., Nelan, J., & Bezanson, R. 2009, AJ, 138, 1417
Tamura, N., Kobayashi, C., Arimoto, N., Kodama, T., & Ohta, K. 2000, AJ, 119, 2134
Trujillo, I., et al. 2006, ApJ, 650, 18
Vader, J. P., Vigroux, L., Lachieze-Rey, M., & Souviron, J. 1988, A&A, 203, 217
van Dokkum, P. G. 2005, AJ, 130, 2647
van Dokkum, P. G., et al. 2008, ApJ, 677, L5
van Dokkum, P. G., et al. 2009, PASP, 121, 2
van Dokkum, P. G., et al. 2010, ApJ, 709, 1018
Wake, D. A., et al. 2008, MNRAS, 387, 1045
Worthey, G., Faber, S. M., & Gonzalez, J. J. 1992, ApJ, 398, 69
Zheng, Z., Zehavi, I., Eisenstein, D. J., Weinberg, D. H., & Jing, Y. P. 2009, ApJ, 707, 554
Zibetti, S., White, S. D. M., & Brinkmann, J. 2004, MNRAS, 347, 556
Zibetti, S., White, S. D. M., Schneider, D. P., & Brinkmann, J. 2005, MNRAS, 358, 949